Journal of Alloys and Compounds 489 (2010) 188–194

Contents lists available at ScienceDirect

Journal of Alloys and Compounds

journal homepage: www.elsevier.com/locate/jallcom

# Densification behavior of nanocrystalline W–Ni–Fe composite powders prepared by sol-spray drying and hydrogen reduction process

J.L. Fan*, X. Gong, B.Y. Huang, M. Song, T. Liu, J.M. Tian

*State Key Laboratory for Powder Metallurgy, Central South University, Changsha, 410083, PR China*

ARTICLE INFO

*Article history:*
Received 20 July 2009
Received in revised form 8 September 2009
Accepted 9 September 2009
Available online 16 September 2009

*Keywords:*
Nanocrystalline composite powders
93W–4.9Ni–2.1Fe
Yttrium
Densification
Liquid-phase sintering

ABSTRACT

This paper studied the densification behavior of nanocrystalline composite powders of 93W–4.9Ni–2.1Fe (wt.%) and 93W–4.9Ni–2.1Fe–0.03Y synthesized by sol-spray drying and hydrogen reduction process. The X-ray diffraction (XRD) analysis showed that γ-(Ni, Fe) phase was formed in the final obtained powders. Powders morphology characterized by scanning electron microscope (SEM) showed that the 93W–4.9Ni–2.1Fe nanocrystalline composite powders exhibited larger agglomeration and grain size compared with the 93W–4.9Ni–2.1Fe–0.03Y nanocrystalline composite powders. Both kinds of green compacts can obtain full density if sintered at 1410 °C for 1 h. When sintering temperature was above 1410 °C, the sintering density for both compacts decreased rapidly. In addition, the sintering density, densification rate and grain coarsening rate of 93W–4.9Ni–2.1Fe compacts were higher than those of 93W–4.9Ni–2.1Fe–0.03Y. The effect of trace yttrium on the densification behavior of nanocrystalline composite powders was also discussed.



## 1. Introduction

Tungsten heavy alloys (WHAs) are two-phase composites consisting of nearly spherical tungsten particles embedded homogeneously in a ductile matrix with low melting point, such as nickel, iron, copper and cobalt [1–3]. Due to the outstanding combination of the properties related to the bcc tungsten phase and fcc matrix, such as high mechanical properties, thermal conductivity and good corrosion resistance, WHAs are widely used in light bulbs filaments, radiation shields, vibration dampers, kinetic energy penetrators and rocket nozzles in space crafts [4–6]. WHAs are usually fabricated by liquid-phase sintering (LPS) process from micron-sized W–Ni–Fe elemental powder mixtures [7,8], and the obtained tungsten grain size is typically about 20–50 μm in diameter. To date, many techniques have been developed to fabricate these alloys, such as solid-phase sintering or LPS of elemental powders, solid-phase sintering of mechanical alloying powders, metal injection molding and microwave sintering [9–13].

It is well known that fine-grained materials provide many attractive properties including high strength, hardness, toughness and good ductility at low temperature according to Hall–Petch relationship. In particular, the propensity to adiabatic shear deformation of WHAs is related to high strain rates and shear localization, which strongly depends on the grain structures [14]. Hence, obtaining a fine-grained microstructure of WHAs attracts continual interests [15]. Previously, oxide dispersion strengthening (ODS) was proved to be an effective method to refine the grain size of WHAs [16–19]. At present, the grain refinement by controlling the sintering process of nanocrystalline composite powders has attracted increased attentions [20]. The preparation of nanocrystalline W–Ni–Fe composite powders is a primary step for the production of the fine-grained WHAs, since the powder properties remarkably affect the subsequent pressing and densification processes. In addition, sintering densification of nanocrystalline composite powders is a critical step to obtain full density and small grain-sized microstructures, which may be different from the densification behavior of the conventional microscaled powders. In our previous work [20], the preparation of the nanosized W–Ni–Fe powders by the sol-spray drying technique has been investigated. That paper focused on the characterization of the nanosized powders. The sintering behavior and the effect of trace yttria particles (added into the prepared nanosized powders and then mixed by ball milling) on the mechanical properties of the sintered alloys were only discussed briefly.

In this work, sol-spray drying and hydrogen reduction process were preferentially used to prepare nanocrystalline W–Ni–Fe composite powders, since this technique can avoid the introduction of the detrimental impurities, and most importantly, can obtain a product with homogeneous composition distribution. The sintering behavior of the nanocrystalline composite powders at various temperatures and holding times was systematically investigated. In addition, the effects of trace yttrium addition (added as yttrium nitrate, differing from the addition of yttria particles) on the densification behavior of nanocrystalline composite powders and the

* Corresponding author. Tel.: +86 731 88836652; fax: +86 731 8710855.
*E-mail address:* fjl@mail.csu.edu.cn (J.L. Fan).

0925-8388/$ – see front matter © 2009 Published by Elsevier B.V.
doi:10.1016/j.jallcom.2009.09.050

mechanical properties of the sintered alloys have been systematically studied. It should be noted that the highly active yttrium can react with some elements during the sintering process, and thus affect the densification behavior.

## 2. Experimental procedures

The raw materials used in the synthesis of nanocrystalline 93W–4.9Ni–2.1Fe and 93W–4.9Ni–2.1Fe–0.03Y composite powders were ammonium metatungstate (purity > 99.5%), $Ni(NO_3)_2{\cdot}6H_2O$ (analytically pure), $Fe(NO_3)_3{\cdot}9H_2O$ (analytically pure) and $Y(NO_3)_3{\cdot}6H_2O$ (analytically pure). According to the stoichiometric ratios, aqueous solution containing W, Ni and Fe salts were prepared by dissolving the solid metal salts into the deionized water with constant stirring. In order to avoid precipitation, a certain amount of PEG-2000 was added into the aqueous solution. Then, nanocrystalline composite powders were obtained by a multi-step process, consisting of sol-spray drying of the precursor solution at 250–350 °C with a solution feed rate of 40–50 ml/min, calcining at 600 °C for 2 h and subsequent reducing by two-step hydrogen reduction process (at 450 °C for 1.5 h and then 850 °C for 1.5 h) in flowing hydrogen atmosphere (dew point of −40 °C). The nanocrystalline 93W–4.9Ni–2.1Fe composite powders with 0.03 wt.% yttrium addition was prepared by the same processes as mentioned above. Since only an imperceptible amount of yttrium exists in the original aqueous solution, the influence of yttrium addition on stoichiometric ratios of the final as-received alloys was negligible.

The nanocrystalline composite powders were die-pressed under 400 MPa for 1 min to form I-shaped samples and the green compacts have a relative density of about 40%. Then, the green compacts were sintered in molybdenum wire furnace under flowing hydrogen atmosphere (dew point of −40 °C) at 900–1460 °C for different holding time. The heating rate was 5 °C/min and the cooling rate to room temperature was 10 °C/min. It should be noted that the present work focused on the densification behavior of the nanocrystalline composite powders and all the obtained data were based on the sintered alloys. The effects of the heat treatment on the microstructures and mechanical behaviors of the sintered compacts will be studied in the future.

The obtained nanocrystalline composite powders were analysed by X-ray diffraction technique (XRD, D/max 2550/Japan). The powders morphology and the sintered compacts were characterized by scanning electron microscope (SEM, JSM-5600LV) and transmission electron microscope (TEM, JEM-200CX). The densities of the sintered compacts were measured by Archimedes' principle. A Nitrogen/Oxygen/Hydrogen Determination (TCH-600, USA) was employed to determine the oxygen contents in the sintered alloys. Hardness of the sintered compacts was determined by means of digital microhardness tester (HXD-1000T).

## 3. Results and discussion

### 3.1. Characteristics of nanocrystalline W–Ni–Fe composite powders

Fig. 1 compares the XRD patterns of the nanocrystalline 93W–4.9Ni–2.1Fe and 93W–4.9Ni–2.1Fe–0.03Y composite powders. It can be seen that only one set of the sharp peaks belonging to bcc-structured tungsten phase are present. However, relatively weak peaks corresponding to γ-(Ni, Fe) phase are also observed in the XRD patterns, indicating that Ni–Fe solid solution formed during sol-spray drying and hydrogen reduction process. This means that composite powders are well synthesized by this method. The products are essentially pure W, Ni and Fe without any detectable oxide phases or other impurities that may come from the raw materials or the following preparation processes. The oxygen contents are 0.059 wt.% for nanocrystalline 93W–4.9Ni–2.1Fe composite powders and 0.23 wt.% for nanocrystalline 93W–4.9Ni–2.1Fe–0.03Y composite powders, respectively. It is emphasized that impurities in 93W–4.9Ni–2.1Fe powders, especially oxygen contents, have been effectively controlled during the fabrication process. However, oxygen contents are very high in 93W–4.9Ni–2.1Fe–0.03Y powders due to the strong affinity between yttrium and oxygen. It should be noted that the peaks of yttrium-containing phase are not observed in the patterns as the result of small amount of yttrium additions. The grain sizes of these nanocrystalline composite powders are determined from XRD patterns by applying the Scherrer equation [21] based on no lattice distortion:

$$d = \frac{0.9\lambda}{\beta\cos\theta} \quad (1)$$

where $d$ is the grain size, $\lambda$ is the X-ray wavelength, $\beta$ is the line width at one-half the maximum intensity, and $\theta$ is the diffraction angle. It should be noted that no lattice strain effects are considered during the grain size calculation because the nanocrystalline composite powders in the present study are produced by gas-phase evaporation, different a lot from the nanocrystalline W–Ni–Fe composite powder synthesized by mechanical alloying process with large lattice distortion, supersolidus solution and amorphous phase [22,23]. Hence, according to Scherrer equation, the calculated tungsten grain sizes of 93W–4.9Ni–2.1Fe and 93W–4.9Ni–2.1Fe–0.03Y powders are about 40–50 nm and 20–30 nm, respectively. Note that the tungsten grain size of 93W–4.9Ni–2.1Fe powders is larger than that of 93W–4.9Ni–2.1Fe–0.03Y powders, indicating significant grain refinement caused by the addition of trace yttrium. Our previous work [24] indicated that the $Y_2WO_6$ compound was formed during hydrogen reduction process by adding 5 wt.% yttrium, and this compound effectively decreased the tungsten grain size of nanocrystalline composite powders through inhibiting the evaporation–sedimentation of tungsten-oxide in hydrogen reduction process. In this work, however, $Y_2WO_6$ diffraction peaks are absent in the XRD patterns due to the small amount of this compound in the nanocrystalline composite powders.

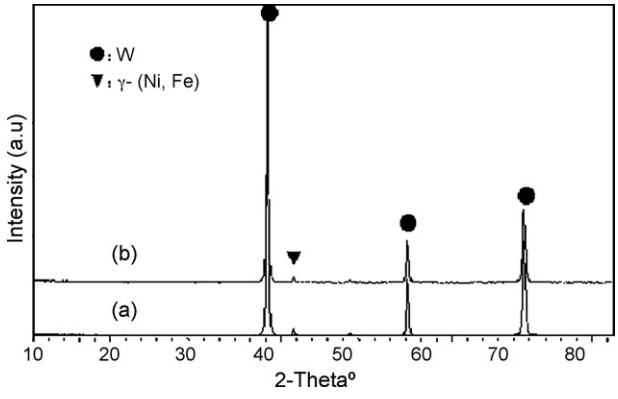


**Fig. 1.** XRD patterns of nanocomposite powders obtained by sol-spray drying and hydrogen reduction process:(a) 93W–4.9Ni–2.1Fe; (b) 93W–4.9Ni–2.1Fe–0.03Y.

The SEM images in Fig. 2 show the morphology of the nanocrystalline composite powders. It can be seen that both powders have a spherical shape and uniform particle size. Agglomeration is also observed in these powders, resulting from the large surface area of the small particles. However, the degree of agglomeration in nanocrystalline 93W–4.9Ni–2.1Fe–0.03Y composite powders is much lower than that in the nanocrystalline 93W–4.9Ni–2.1Fe composite powders. The reason may be that the $Y_2WO_6$ compounds are homogeneously adsorbed on the surfaces of these nanosized particles and significantly reduce the surface activity.

### 3.2. Sintering densification and microstructure evolution of nanocrystalline 93W–4.9Ni–2.1Fe composite powders

Fig. 3 plots the sintering density of 93W–4.9Ni–2.1Fe compacts versus sintering temperature at different holding time. It can be seen that the density increases gradually when the sintering temperature increases from 1320 °C to 1410 °C and nearly full density (17.646 g/cm$^3$) is obtained at 1410 °C for 1 h (the theoretical density is 17.735 g/cm$^3$). When the sintering temperature is above 1410 °C, the fully dense compacts are subject to density degradation with increasing sintering temperature. The trend of density degradation becomes more obvious as the holding time increases. For instance, the sintering density of the 93W–4.9Ni–2.1Fe compacts decreases

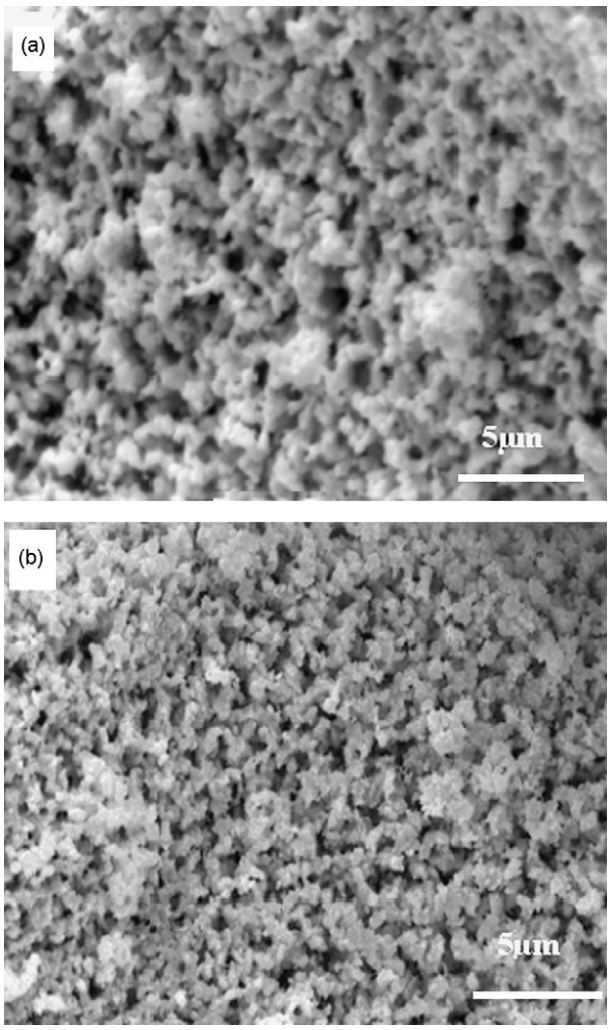


**Fig. 2.** SEM micrographs of nanocomposite powders after hydrogen reduction: (a) 93W–4.9Ni–2.1Fe; (b) 93W–4.9Ni–2.1Fe–0.03Y.

from 17.646 g/cm$^3$ (99.5% of theoretical density) at 1410 °C for 1 h to 17.5 g/cm$^3$ (98.7% of theoretical density) at 1460 °C for 1 h, and further decreases to 17.37 g/cm$^3$ (98.0% of theoretical density) at 1460 °C for 1.5 h. Moreover, at the same sintering temperature, increasing sintering time will be beneficial to obtain high density if the temperature is below 1410 °C. However, it should be noted that long holding time is detrimental to obtain a fine-grained microstructure. Hence, the following sintering experiments are all performed at the same holding time of 1 h.

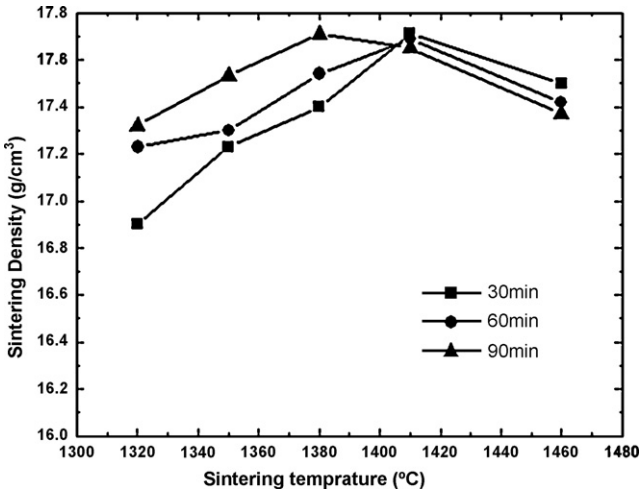


**Fig. 3.** Sintering densities of 93W–4.9Ni–2.1Fe compacts as a function of the sintering temperature at different holding time of 30 min, 60 min, and 90 min.

Fig. 4 shows the microstructure of the sintered 93W–4.9Ni–2.1Fe compacts at 1320 °C, 1380 °C, 1410 °C, and 1460 °C for 1 h. When sintered at 1320 °C and 1380 °C for 1 h, only trace Ni–Fe matrix forms (indicated from the white area) and a lot of pores still exist (marked by arrows) as shown in Fig. 4(a) and(b). The tungsten grains with an average size of 2–5 μm have not been penetrated by the matrix and their shapes are irregular. These features indicate that liquid-phase sintering has not started at 1320 °C or 1380 °C. During this sintering stage, densification strongly depends on necks development among tungsten particles through grain boundary diffusion. Many pores will form on tungsten grain boundaries if sintering time is not long enough for tungsten atoms to diffuse sufficiently. And only a limited sintering density can be obtained by solid-phase sintering. When sintered at 1410 °C, significant changes in the microstructure are observed (Fig. 4(c)). The porosity is eliminated completely and 99.5% of the theoretical density is obtained. Tungsten grains are penetrated by the Ni–Fe matrix and become more round. These grains have a remarkable growth from 2–5 μm up to 10–20 μm and are distributed uniformly in the continuous matrix, indicating the start of liquid-phase sintering. Once the liquid-phase appears, the enhanced dissolution-precipitation and rearrangement mechanisms dominate the densification behavior. Grain coarsening, grain shape accommodation, pores elimination and W–W contiguity reduction will proceed very quickly and a fully dense microstructure will be achieved. However, the failure of tungsten grains is predominated by intergranular cracking as well as a few matrix ductile rupture, indicating the weakness in the tungsten/matrix interfacial bonding. Mechanical properties of the obtained samples are 950 MPa in tensile strength and 12% in elongation. Moreover, many undissolved tungsten particles with an average size of about 5 μm locating along the tungsten grain boundaries confirm the insufficient liquid-phase sintering. However, a further increase in sintering temperature to 1460 °C results in the disappearance of these small particles as well as a continuous grain growth because of the persistent migration of grain boundaries in higher temperature. And the average tungsten grain size is about 20–50 μm, as shown in Fig. 4(d). In particular, some pores and micro-cracks (marked by arrows) are also formed in these compacts. These sintering defects directly lead to lower sintering density (Fig. 3) and lower properties (tensile strength is 830 MPa and elongation is 10%) compared with the alloy sintered at 1410 °C for 1 h, although a few transgranular cleavages can be clearly observed in the fracture surface. The anomalous decrease in sintering density and properties after full densification is possibly ascribed to the trapped gases within the residual pores. As the temperature increases, pressure of trapped gases in pores expands and impedes liquid-phase to fill them. If cooling rate is too fast, these pores will be retained and result in the low sintering density and properties.

Due to the absence of the heat treatment to remove the residual hydrogen after the sintering, the mechanical properties of the alloys in the present study are relatively lower than those of the conventional WHAs with the similar compositions, as shown in some literatures [25,26]. However, the mechanical properties (950 MPa in tensile strength and 12% in elongation) are still impressive since the sintered compacts are not soaked in an inert atmosphere to eliminate the “hydrogen brittleness”. If the process was integrated with a proper hydrogen-elimination treatment, it is believed that the mechanical properties of the alloy will be further improved.

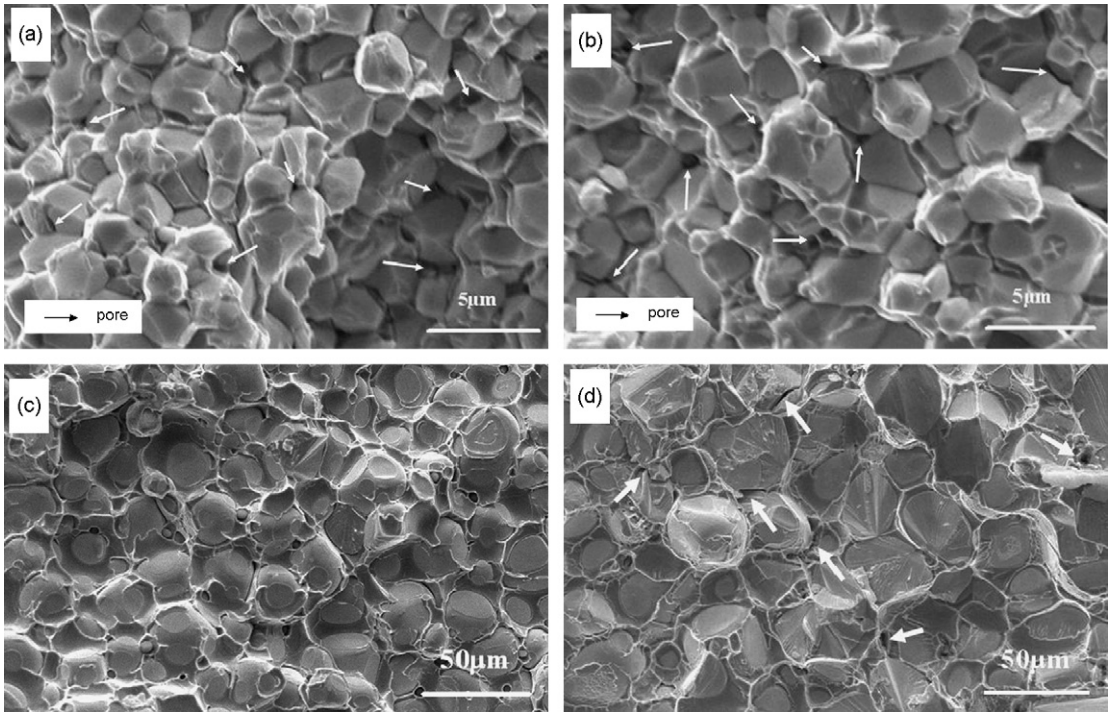


**Fig. 4.** SEM fractographs of 93W–4.9Ni–2.1Fe sintered compacts at different temperature for 1 h: (a) 1320 °C; (b) 1380 °C; (c) 1410 °C; (d) 1460 °C.

Generally, the typical LPS temperature of the conventional WHAs with coarse grains is about 1450 °C due to the poor sintering activity of micron-sized powders. In this study, the appearance of liquid-phase and nearly full density occur at a lower temperature of 1410 °C. The decreased LPS temperature is mainly attributed to the larger surface area of the grain boundaries and the high surface energy in the raw nanocrystalline composite powders. During heating, the numerous grain boundaries act as the fast paths for atoms and vacancies diffusion and the large surface energy provided by the nanoscaled particles also aids the sintering driving force. As a consequence, obvious densification can be obtained at a lower temperature of 1410 °C.

### 3.3. *Effect of trace yttrium addition on densification behavior of nanocomposite powders*

Fig. 5 displays the relationship between the relative density of 93W–4.9Ni–2.1Fe and 93W–4.9Ni–2.1Fe–0.03Y compacts and the sintering temperature. It has been shown that the densities of both compacts increase with the sintering temperature from 900 °C to 1410 °C, and decrease with the sintering temperature when the sintering temperature is above 1410 °C. Densification rate is very rapid when the temperature is below 1200 °C and significant densification occurs by solid-phase sintering prior to liquid-phase formation. It is worth noting that the relative densities of 93W–4.9Ni–2.1Fe–0.03Y compacts are always lower than that of 93W–4.9Ni–2.1Fe compacts, indicating that the addition of trace yttrium can inhibit densification behavior.

Fig. 6 shows that the microstructure of the 93W–4.9Ni–2.1Fe–0.03Y compacts sintered at 1320 °C, 1380 °C, 1410 °C, and 1460 °C for 1 h. It can be seen that the densification tendency and microstructure evolution are similar to 93W–4.9Ni–2.1Fe–0.03Y compacts when the sintering temperature is below 1410 °C. When sintered at 1410 °C, many undissolved small tungsten particles distribute among the large tungsten grains as shown in Fig. 6(c). These undissolved particles are not eliminated completely by grain boundaries migration when the sintering temperature is elevated to 1460 °C, as marked by the arrows in Fig. 6(d). The tungsten grains fail predominately by intergranular cracking and the mechanical properties of the sintered alloys are 895 MPa, 840 MPa in tensile strength, and 15%, 8% in elongation for the compacts sintered at 1410 °C and 1460 °C, respectively. Furthermore, at the same sintering temperature for holding 1 h, average grain sizes are slightly smaller than that of 93W–4.9Ni–2.1Fe compacts regardless of some extremely large grains in Fig. 6(d). In order to investigate the effect of trace yttrium on grain growth in detail, the sintering experiments are conducted at different sintering temperatures with the same holding time of 1 h, and the results are plotted in Fig. 7. It can be seen that both kinds of compacts have no obvious grain growth and have the same grain coarsening rate when the sintering temperature

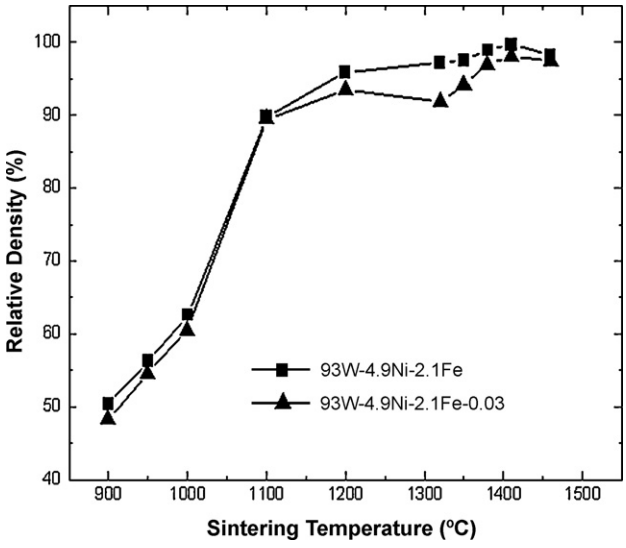


**Fig. 5.** Comparison of relative densities versus the sintering temperature by holding 1 h: ■, 93W–4.9Ni–2.1Fe; ▲, 93W–4.9Ni–2.1Fe–0.03Y.

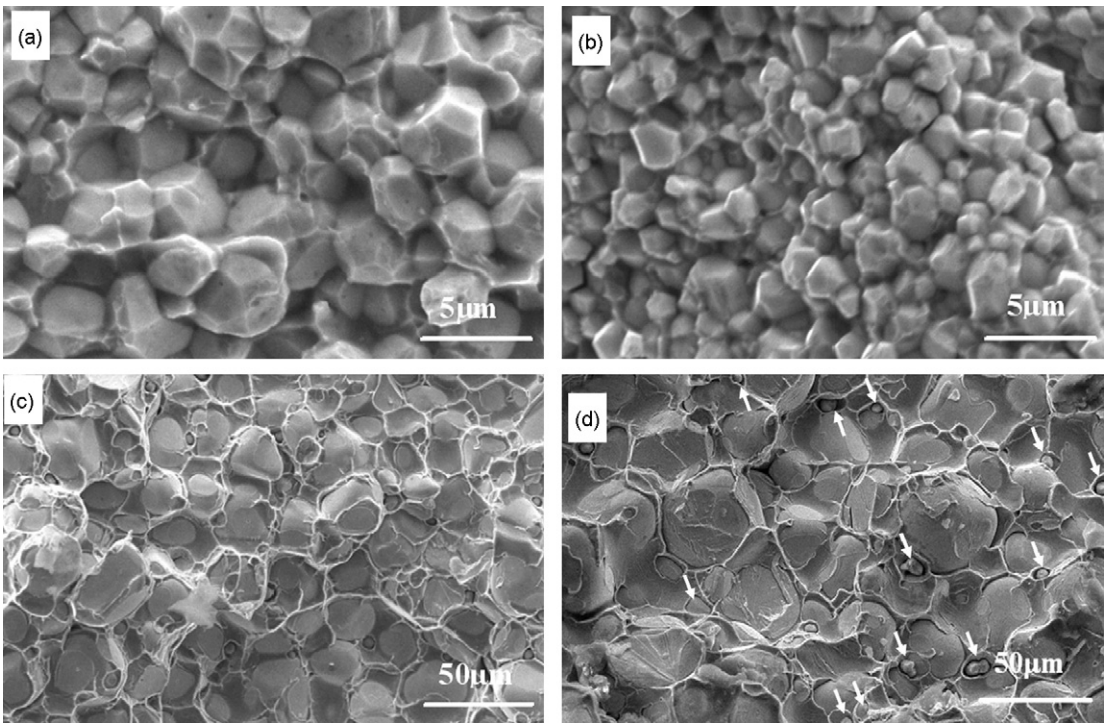


**Fig. 6.** SEM fractographs of 93W–4.9Ni–2.1Fe–0.03Y sintered compacts at different temperature for 1 h: (a) 1320 °C; (b) 1380 °C; (c) 1410 °C; (d) 1460 °C.

is below 1380 °C. However, a significant increase of the grain size occurs in both compacts when the temperature is above 1380 °C, as a consequence of liquid-phase appearance and the enhanced solution-precipitation process. In addition, compared with the compacts of 93W–4.9Ni–2.1Fe, grain coarsening rate of the 93W–4.9Ni–2.1Fe–0.03Y compacts is much lower when sintered at a temperature above 1380 °C. This further validates that trace yttrium addition affects the sintering behavior of nanocrystalline composite powders, especially during the liquid-phase sintering period.

During liquid-phase sintering, the kinetic equation of grain coarsening can be expressed as [27]:

$$G^n = G_0^n + Kt \quad (2)$$

where $G$ is the tungsten grain size, $G_0$ is the initial tungsten grain size, $n$ generally equals to 3 for tungsten heavy alloys, $t$ is isothermal time and $K$ is the grain coarsening rate. The relationship between the grain size and holding time are plotted under a sintering temperature of 1410 °C, as shown in Fig. 8. The calculated values of the grain coarsening rates obtained from the slopes of the fitted lines are 76 $\mu m^3$/min and 23 $\mu m^3$/min, respectively. For 93W–4.9Ni–2.1Fe compacts, the calculated grain coarsening rate is more than three times higher than that of 93W–4.9Ni–2.1Fe–0.03Y compacts. The obvious difference in grain coarsening rate indicates that the sintering densification of 93W–4.9Ni–2.1Fe–0.03Y compacts is substantially inhibited.

TEM bright-field image of 93W–4.9Ni–2.1Fe–0.03Y compacts after sintered at 1410 °C for 1 h reveals that one heterogeneous particle about 1 μm in diameter distributes in the matrix (shown

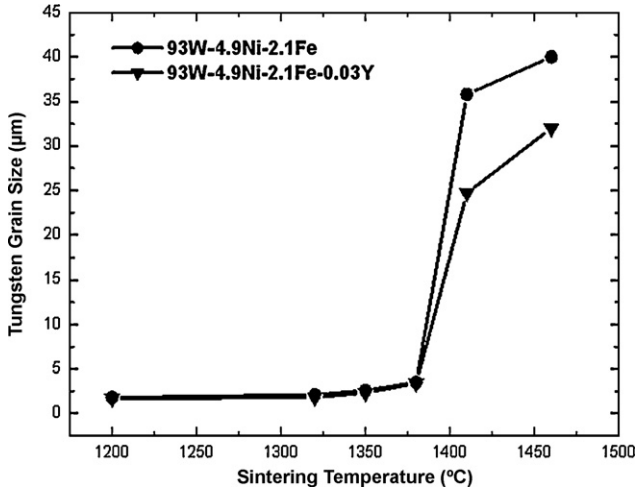


**Fig. 7.** Grain size as a function of the sintering temperature for the same holding time of 1 h: ●, 93W–4.9Ni–2.1Fe; ▼, 93W–4.9Ni–2.1Fe–0.03Y.

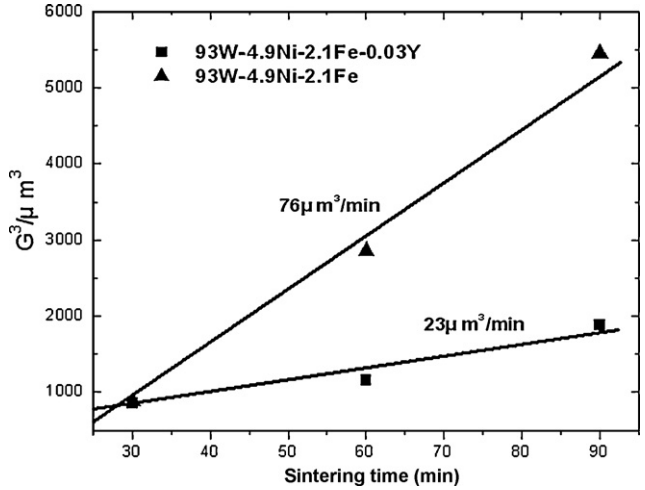


**Fig. 8.** Comparison of calculated grain coarsening rates after sintered at 1410 °C for different holding time: ▲, 93W–4.9Ni–2.1Fe; ■, 93W–4.9Ni–2.1Fe–0.03Y.

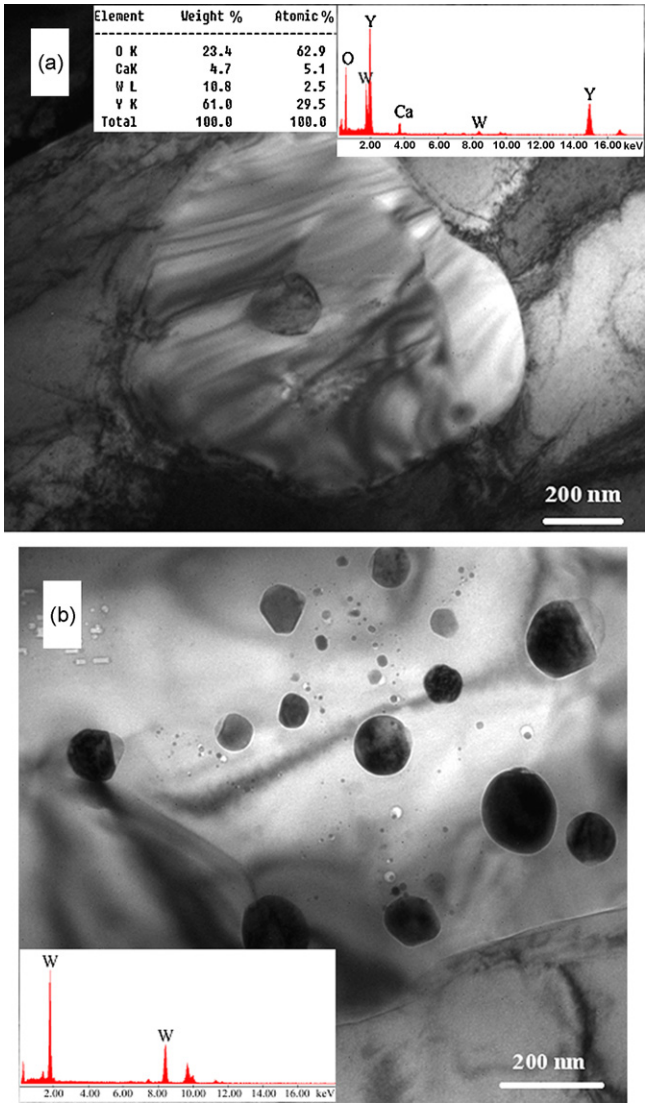


**Fig. 9.** TEM bright-field (BF) images of 93W–4.9Ni–2.1Fe–0.03Y alloy after sintered at 1410 °C for 1 h: (a) one particles locates in the matrix and the EDS analysis (indicated in the inset) shows that its composition mainly consists of yttrium and oxygen; (b) many nanoscaled tungsten particles are adjacent to the yttrium-containing particles and their composition is determined by the EDS analysis, as shown in the inset in (b).

in Fig. 9(a)). The EDS analysis indicates that the chemical composition of the particle consists of yttrium and oxygen with a little impurity of calcium, illuminated by the inset in Fig. 9(a). The high oxygen contents in the yttrium-containing particle imply that the addition of trace yttrium can react with the oxygen element in the sintered alloy. At high temperature, the solubility of interstitial elements (oxygen) in tungsten lattice is high, but the impurity elements are prone to segregate along the grain boundaries during cooling, thereby significantly weakening the grain boundary strength. The addition of highly active yttrium plays a role in purifying and strengthening the grain boundaries.

The oxygen contents in the sintered compact are determined by a special instrument with a very high precision and the result shows that the residual oxygen contents are around 0.0082 wt.%. Due to the high homogeneity in the original powder, there is no doubt that the added 0.03 wt.% yttrium distribute homogeneously in the sintered compact. Hence, the atoms ratio of yttrium to oxygen can be estimated and the value is approximately 2:3 (the weight percent of oxygen is about 21.5%), which is in good agreement with the stoichiometric ratio of $Y_2O_3$. In addition, the binary phase diagram of Y–O system also shows that the 21.5 wt.% oxygen corresponds to the phase field of $Y_2O_3$, indicating that the yttrium-containing particle may be yttria in the view of thermodynamics. Nevertheless, the above speculation is limited. In order to identify the phase structure of the unknown particle precisely, the Selected Area Electron Diffraction (SAED) will be conducted in the near future.

The above discussion implies that the initial addition of $Y(NO_3)_3{\cdot}6H_2O$ has been transformed into the yttrium-containing particles via a series of complex chemical reactions and these reactions may substantially influence the densification behavior. In particular, the compound of $Y_2WO_6$ may suffer from decomposition or other changes during the sintering process, because the weight ratio of the elements (yttrium and oxygen) in the sintered alloy, determined by the EDS analysis or the high precision analysis, deviates a lot from the stoichiometric ratio of the $Y_2WO_6$. The possible chemical reaction can be described as follows: $Y_2WO_6 + 3H_2 \rightarrow Y_2O_3 + W + 3H_2O$. Although the phase transformation of trace yttrium addition in the powder preparation process has been systematically investigated in our previous work [24], the reaction mechanism in the sintering process is still not clear and needs a further study.

Throughout the sintering process, the diffusion of tungsten atoms to γ-(Ni, Fe), especially in the liquid-phase stage, may be strongly disturbed due to part of the tungsten atoms participating in the reactions with yttrium. The formation of some unknown compounds containing yttrium during the sintering process may result in the decrease in the wettability of the liquid-phase on tungsten particles. In addition, the yttrium-containing particles are partially responsible for the inhibition of mass flow in solution-precipitation process. Thus, the density of the sintered compacts and the grain coarsening rate differ a lot from those of compared with the compacts without yttrium addition (Fig. 8) in spite of the low volume fraction of yttrium addition.

In addition, Fig. 9(b) shows that many nanoscaled particles, embedded in the region adjacent to the yttrium-containing particle, are found to have very high tungsten contents and with no nickel or iron contents, determined by EDS analysis (see the inset in Fig. 9(b)). The formation of these nanoscaled tungsten particles is associated with incomplete solution-precipitation process during the liquid-phase sintering. Because the yttrium-containing particles locate in the matrix, the rate of solution-precipitation is inhibited by blocking the mass flow diffusion from solid-phase to liquid-phase. As a result, many smaller grains, especially those close to the yttrium-containing particles, which should have been expended to maintain progressive growth of larger grains (this process is usually termed as Ostwald ripening) are retained eventually. Furthermore, these inhibitors of yttrium-containing particles also cause a decrease in the grain coarsening rate so that the compacts with trace yttrium addition obtain a smaller tungsten grain size and lower densification. The final obtained specimens after sintered at 1410 °C or 1460 °C for 1 h show that 93W–4.9Ni–2.1Fe–0.03Y compacts generate obvious bending while no bending or other distortion has been observed in the sintered 93W–4.9Ni–2.1Fe compacts (the images of the sintered specimens are not shown here). On account of high oxygen contents (0.23 wt.%) in 93W–4.9Ni–2.1Fe–0.03Y compacts, it is reasonable to believe that the bending distortion or swelling is at least partly due to the formation of water vapor during liquid-phase sintering under hydrogen atmosphere as a consequence of the reaction between hydrogen and oxygen.

The hardness as a function of the sintering temperature at the same holding time for 93W–4.9Ni–2.1Fe and 93W–4.9Ni–2.1Fe–0.03Y compacts is plotted in Fig. 10. It can be seen that the hardness significantly increases with the increase in the temperature. However, the hardness decreases much more obviously when the temperature exceeds 1410 °C. The

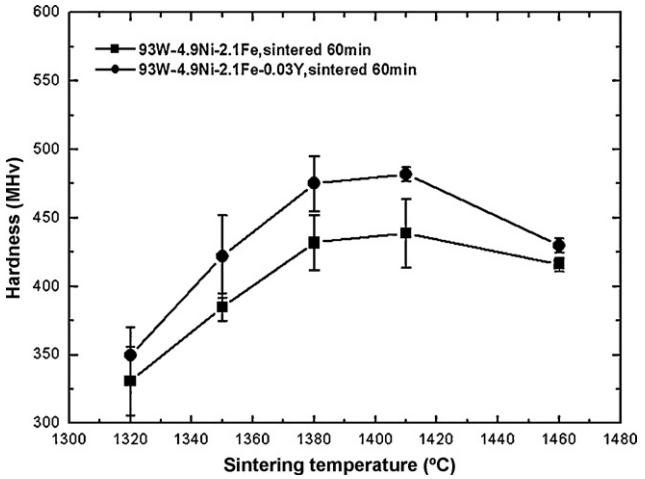


**Fig. 10.** Hardness as a function of the sintering temperature at the same holding time of 1 h: ■, 93W–4.9Ni–2.1Fe; ●, 93W–4.9Ni–2.1Fe–0.03Y.

maximum hardness can be increased up to **Hv**439 ± 25 for 93W–4.9Ni–2.1Fe alloy and **Hv**482 ± 5 for 93W–4.9Ni–2.1Fe–0.03Y alloy after sintered at 1410 °C for 1 h. In addition, though 93W–4.9Ni–2.1Fe–0.03Y alloy has lower sintering density compared to 93W–4.9Ni–2.1Fe alloy (Fig. 5), it shows a much higher hardness than that of 93W–4.9Ni–2.1Fe alloy in the same sintering condition, probably due to the hard yttrium-containing ceramic particles and the formation of nanoscaled tungsten particles.

## 4. Conclusion

In this paper, densification behavior of nanocomposite powders of 93W–4.9Ni–2.1Fe and 93W–4.9Ni–2.1Fe–0.03Y has been investigated. The following conclusions can be drawn:

(1) XRD reveals that fcc γ-(Ni, Fe) phase is formed in the final obtained nanocrystalline composite powders, indicating that composite powders are well synthesized by sol-spray drying and hydrogen reduction process. Compared with the nanocrystalline 93W–4.9Ni–2.1Fe composite powders, nanocrystalline 93W–4.9Ni–2.1Fe–0.03Y composite powders exhibit lower agglomeration and smaller tungsten grain size, resulted from the addition of trace amount of yttrium.
(2) The sintering density and grain size of the two nanocrystalline composite powder compacts exhibit an increasing tendency with the sintering temperature up to 1410 °C but an inverse trend when the temperature exceeds 1410 °C. The appearance of liquid-phase and evident densification occur at 1410 °C, and fully dense microstructure is obtained at 1410 °C for 1 h.
(3) In comparison with the sintered 93W–4.9Ni–2.1Fe compacts, 93W–4.9Ni–2.1Fe–0.03Y compacts exhibit lower sintering density, densification rate, grain size and grain coarsening rate. TEM observation shows that the yttrium-containing particles distribute in the matrix and many nano tungsten particles locate at the region adjacent to the yttrium-containing particles.
(4) The hardness of 93W–4.9Ni–2.1Fe and 93W–4.9Ni–2.1Fe–0.03Y compacts shows an increasing tendency with the sintering temperature and the maximum hardness can reach **Hv**439 ± 25 and **Hv**482 ± 5, respectively. However, the hardness decreases considerably when the temperature exceeds 1410 °C. The higher hardness in 93W–4.9Ni–2.1Fe–0.03Y compacts may result from the formation of nano tungsten particles and hard yttrium-containing ceramic particles.

## Acknowledgements

This research work is supported by National Nature Science Foundation of China (Grant No. 50674106), National Natural Science Funds for Distinguished Young Scholars (No.50925416) and Creative research group of National Nature Science Foundation of China (Grant No. 50721003).

## References

[1] H.J. Ryu, S.H. Hong, W.H. Baek, Mater. Sci. Eng. A 291 (2000) 91–96.
[2] A. Upadhyaya, Mater. Chem. Phys. 67 (2001) 101–110.
[3] A. Sunwoo, S. Groves, D. Goto, Mater. Lett. 60 (2006) 321–325.
[4] I.S. Humail, F. Akhtar, S.J. Askari, Int. J. Refract. Met. Hard Mater. 25 (2007) 380–385.
[5] R. Gero, L. Borukhin, I. Pikus, Mater. Sci. Eng. A 302 (2001) 162–167.
[6] M. Bahgat, M.K. Paek, J.J. Pak, J. Alloys Compd. 472 (2009) 314–318.
[7] R.M. German, K.S. Churn, Metall. Trans. A 15 (1984) 747.
[8] A. Upadhyaya, S.K. Tiwari, P. Mishra, Scripta Mater. 56 (2007) 5–8.
[9] Z.W. Zhang, J.E. Zhou, S.Q. Xi, Mater. Sci. Eng. A 379 (2004) 148–153.
[10] Y.W.R.M. German, B. Marx, J. Mater. Sci. 38 (2003) 2271–2281.
[11] J.L. Fan, B.Y. Huang, X.H. Qu, Int. J. Refract. Met. Hard Mater. 19 (2001) 73–77.
[12] B.Y. Huang, J.L. Fan, S.Q. Liang, J. Mater. Process. Technol. 137 (2003) 177–182.
[13] C.S. Zhou, J.H. Yi, S.D. Luo, J. Alloys Compd. 482 (2009) L6–L8.
[14] Q. Wei, T. Jiao, K.T. Ramesh, Acta Mater. 54 (2006) 77–87.
[15] J.L. Fan, T. Liu, H.C. Chen, J. Mater. Process. Technol. 208 (2008) 463–469.
[16] S. Park, D.K. Kim, S. Lee, H.J. Ryu, S.H. Hong, Metall. Trans. A 32 (2001) 2011–2020.
[17] H.J. Ryu, S.H. Hong, Mater. Sci. Eng. A 363 (2003) 179–184.
[18] K.H. Lee, S.I. Cha, H.J. Ryu, M.F. Dilmore, S.H. Hong, J. Alloys Compd. 434–435 (2007) 433–436.
[19] K.H. Lee, S.I. Cha, H.J. Ryu, S.H. Hong, Mater. Sci. Eng. A 452–453 (2007) 55–60.
[20] J.L. Fan, T. Liu, Y.Z. Ma, Mater. Sci. Forum 534–536 (2007) 1409–1412.
[21] B.D. Cullity, S.R. Stock, Elements of X-Ray Diffraction, third ed., Prentice Hall, 2001, pp. 167–170.
[22] J.L. Fan, B.Y. Huang, J. Adv. Mater. 36 (2004) 48–52.
[23] Z.W. Zhang, J.E. Zhou, S.Q. Xi, G. Ran, J. Alloys Compd. 370 (2004) 186–191.
[24] S.G. Peng, J.L. Fan, T. Liu, Mater. Sci. Eng. Powder Metall. 2 (2008) 106–110 (Chinese).
[25] I.S. Humail, F. Akhtar, S.J. Askari, Int. J. Refract Met. Hard Mater. 25 (2007) 380–385.
[26] S. Eroglu, T. Baykara, J. Mater. Process. Technol. 103 (2000) 288–292.
[27] R.M. German, Sintering Theory and Practice, Wiley, New York, 1996, p. 163.